

# A muon scattering tomography system based on high spatial resolution scintillating detector

Zheng Liang<sup>a</sup>, Zebo Tang<sup>a</sup>, Xin Li<sup>b</sup>, Baiyu Liu<sup>a</sup>, Cheng Li<sup>a</sup>, Jiacheng He<sup>a</sup>, Kun Jiang<sup>c</sup>, Yonggang Wang<sup>a</sup>, Ye Tian<sup>b</sup>, Yishuang Zhang<sup>a</sup>, Zeyu Wang<sup>a</sup>

<sup>a</sup>*Department of Modern Physics, University of Science and Technology of China, Hefei, 230026, Anhui, China*

<sup>b</sup>*Institute of Modern Physics, Chinese Academy of Sciences, Lanzhou, 730000, Gansu, China*

<sup>c</sup>*Institute of Deep Space Sciences, Deep Space Exploration Laboratory, Hefei, 230026, China*

---

## Abstract

Cosmic ray muon scattering tomography (MST) is an imaging technique that utilizes muon scattering in matter to inspect high-Z materials non-destructively, without requiring an artificial radiation source. This method offers significant potential for applications in border security and long-term monitoring of nuclear materials. In this study, we developed a high-precision plastic-scintillator-based position-sensitive detector with a spatial resolution of 0.09 times the strip pitch. A fully functional, full-scale imaging system was then constructed using four layers of such XY position-sensitive detectors, each with an effective area of 53 cm × 53 cm. This paper details the following key contributions: the Geant4-simulated design and optimization of the imaging system, the fabrication, assembly, and testing of the detectors, and an evaluation of the imaging performance of the completed system.

*Keywords:*

Muon scattering tomography, Plastic scintillation detectors, Cosmic ray muon tracking

---

*Email addresses:* zbtang@ustc.edu.cn (Zebo Tang), lixin@impcas.ac.cn (Xin Li)

## 1. Introduction

Cosmic ray muons, naturally occurring and highly penetrating particles, serve as a unique tool for non-destructive imaging, leading to two primary techniques: muon transmission radiography and muon scattering tomography. Transmission radiography, which measures the attenuation of muon flux, has been successfully used to image internal density structures of large-scale objects, such as volcanoes [1, 2] and archaeological structures [3]. In contrast, scattering tomography, which reconstructs the multiple Coulomb scattering angles of muons, is particularly sensitive to atomic number ( $Z$ ) and has become a promising method for detecting high- $Z$  materials, such as in the control of special nuclear materials for border security [4, 5, 6, 7].

Although they have different principles and applications, both muographic techniques face a shared fundamental challenge: building a robust, large-area position-sensitive tracker with high spatial resolution. The efficiency and quality of the final image directly depend on the performance of these tracking detectors.

In the field of particle detection and imaging, the selection of detector technology often involves a trade-off among performance, cost, and deployability. Among the available options, plastic scintillator detectors read out by silicon photomultipliers (SiPMs) offer a compelling solution for practical field deployment, primarily due to their exceptional operational stability and environmental robustness. Unlike gaseous detectors such as drift chambers[8], Micromegas[9], or resistive plate chambers (RPCs)[10], they do not require gas circulation systems or high-voltage infrastructure. However, conventional plastic scintillator detectors are typically associated with two major limitations: prohibitive cost for large-area coverage and spatial resolution inferior to that of gaseous detectors. These inherent challenges motivate the central objective of this work: to develop a large-area plastic scintillator detector that simultaneously achieves reduced cost and improved spatial resolution, thereby enhancing its competitiveness for widespread applications in muon scattering tomography (MST).

To this end, we have designed and fabricated a modular, cost-effective, position-sensitive plastic scintillator detector with high spatial resolution for cosmic-ray muon scattering imaging. The detector achieves a spatial resolution as fine as 0.09 times the strip pitch. Its modular architecture enables seamless expansion of the effective detection area through tiling of multiple units, thus meeting the large-area coverage requirements essential for practi-

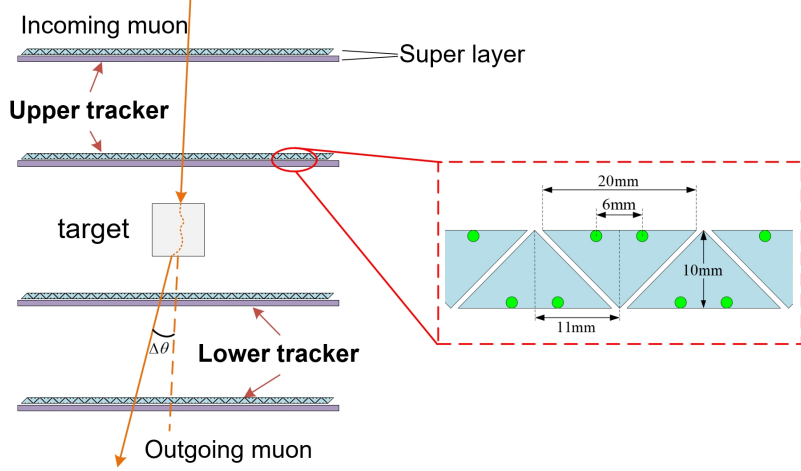


Figure 1: Structural diagram of the Muon Scattering Tomography (MST) system. (Left) Four Super Layers, formed by orthogonally stacking two detection planes, provides the incoming and outgoing muon tracks. (Right) Internal grooving of the scintillator bar with embedded wavelength-shifting (WLS) fiber.

cal MST systems.

## 2. System design

### 2.1. System layout

A typical muon scattering imaging system generally comprises at least four layers of two-dimensional position-sensitive detectors, with two layers placed above and two below the object under inspection. Figure 1 illustrates the layout of our MST system. The upper tracker which records the incident muon trajectories, and the lower tracker which records the outgoing trajectories, each consist of two “Super Layers” that provides two-dimensional position information of the incident particles. By measuring the scattering angles of muons after they penetrate the target, the scattering density distribution of materials within the investigated volume can be reconstructed[6].

Each super layer is composed of two orthogonally oriented one-dimensional detection planes, with each plane providing a one-dimensional position measurement. Each detection plane comprises an array of parallel scintillator bars, such that the specific bars fired in an event determine the muon’s hit position.

Each scintillator bar is wrapped in reflective material and incorporates an internal groove to accommodate a Wavelength-Shifting (WLS) fiber. As a cosmic ray muon passes through the plastic scintillator of the detection plane, it deposits energy—typically several MeV, a value dependent on the scintillator thickness—causing the emission of fluorescent photons. The photons are absorbed by the WLS fiber and subsequently re-emitted. A fraction of these re-emitted photons, falling within the acceptance angle for total internal reflection, are trapped and guided along the fiber. Ultimately, they propagate to the fiber end, where they are converted into electrical signals by the SiPM.

Based on our previous findings that triangular-cross-section scintillator bars significantly enhance detector spatial resolution without decreasing the pitch[11, 12], the current detector design incorporates triangular scintillators to achieve improved spatial resolution.

## 2.2. Imaging simulation

While it is widely acknowledged that enhanced detector resolution improves MST image quality, the exact quantitative relationship is not yet fully established. To quantify this relationship, we conducted a Geant4 simulation to determine the required detector position resolution for the imaging system.

The Geant4 simulation geometry is illustrated in figure 2. Due to the limited height of the imaging system, the inter-layer spacing within both the upper and lower trackers confined to 90 cm. A 20 cm gap was reserved between the upper and lower tracker modules to accommodate the imaging target, which is composed of 10-cm cubes made of iron (Fe), aluminum (Al), copper (Cu) and lead (Pb). The green planes in the diagram represent the detector planes. In this model, the detectors are simplified as homogeneous plastic slabs, omitting internal structure details and scintillation photon production. This approach was adopted to accelerate the simulation without compromising the accuracy in modeling muon scattering through key components, such as plastic scintillator and imaging targets. Muons were generated with initial kinetic energy, position, and incident angle sampled according to the Chatzidakis model[13], and propagated from left to right in the simulation geometry.

In order to model the finite spatial resolution of the detectors, the exact muon hit positions recorded by Geant4 were smeared by adding a random number drawn from a Gaussian distribution. The standard deviation  $\sigma$  of this

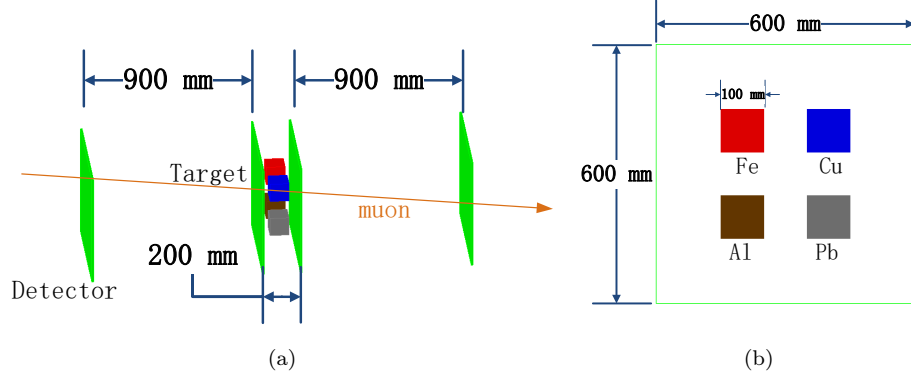


Figure 2: Geant4 geometry setup for imaging simulation.(a) Model of the complete detector structure.(b) Four cubic targets placement.

distribution is defined as the spatial resolution of the detector. To systematically quantify the effect of detector spatial resolution on the reconstructed image, we employed the Point of Closest Approach (PoCA) algorithm[7] for image reconstruction across a range of  $\sigma$  values from 0 mm to 5 mm.

Figure 3 presents the imaging results using the PoCA algorithm under two different detector spatial resolutions ( $\sigma_x = 1$  mm and 3 mm). It can be observed that the impact of detector resolution on the imaging performance is mainly manifested in two aspects: the contrast between the signal and the background, and the sharpness of the object boundaries.

In optical systems, the Point Spread Function (PSF) is defined as the response of the system to an ideal point target[14]. This concept can be extended to muon scattering tomography to quantify the blurring introduced by the finite detector resolution and the reconstruction algorithm itself. The PSF of muon imaging system can be modeled as a Gaussian function  $G(x, \varepsilon)$  with a resolution parameter  $\varepsilon$ . The input to the imaging system, which is the spatial density distribution of the object under investigation, can be approximated as a step function,  $H(x)$ . Consequently, the resulting output image is mathematically described as the convolution of this step function with the Gaussian PSF, which is a error function:

$$f(x) = (H * G) = \frac{1}{2} \left[ 1 + \text{erf} \left( \frac{x}{\sqrt{2\varepsilon}} \right) \right] \quad (1)$$

Therefore, in figures 3c and 3d, the image edges are fitted with an error function to quantitatively analyze the contrast and blurring.

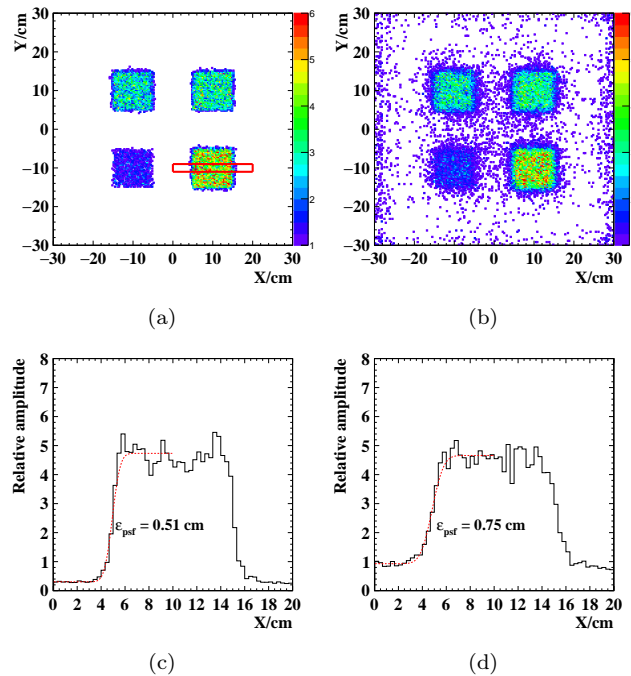


Figure 3: Application of the PoCA algorithm to Geant4 simulation data. (a, b) Reconstructed images for detector spatial resolutions of 1 mm and 3 mm. (c, d) X-axis profiles of the lead brick region ( $5 \text{ mm} < x < 15 \text{ mm}$ ) corresponding to the images above, with error function fit applied to the edge.

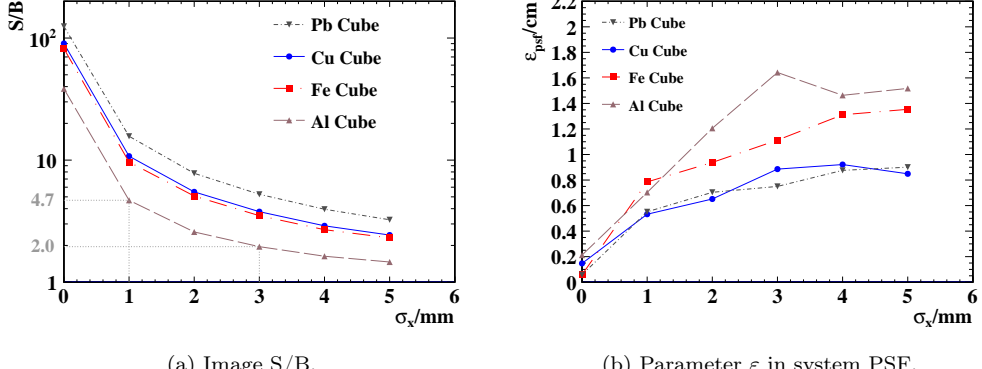


Figure 4: Performance of imaging system with different detector spatial resolutions.

The image contrast is characterized by the signal-to-background ratio (S/B), defined as the ratio of the amplitude in the region-of-interest to that in the background, which is  $A_{\text{sig}}/A_{\text{bkg}}$ [15]. The sharpness of the boundaries in the reconstructed image is characterized by the parameter  $\epsilon$  in equation 1.

Figure 4 shows the performance of imaging systems employing detectors with varying position resolutions. As shown, the image S/B exhibits a marked improvement as the spatial resolution improved. For instance, when the detector spatial resolution  $\sigma_x$  improved from 3 mm to 1 mm, S/B for the aluminum block imaging increased from 2.0 to 4.7. The boundary sharpness, while also affected by the spatial resolution, exhibits a less pronounced dependence compared to the S/B.

MST systems based on scintillator detectors commonly achieve a spatial resolution around 3 mm[16]. The Geant4 simulation results demonstrate that while a 3 mm spatial resolution can successfully image low-Z elements like aluminum, the resulting image quality is substantially limited, highlighting the need for superior resolution. This provides a critical reference for our detector design specifications: the spatial resolution should be aimed for as close to 1 mm as possible.

### 2.3. Scintillating detector

#### 2.3.1. Design and optimization

A conventional position-sensitive scintillator detector is typically fabricated by assembling long scintillator bars into a detection plane. The cross-sectional geometry of the scintillator bars strongly affects the detector's spa-

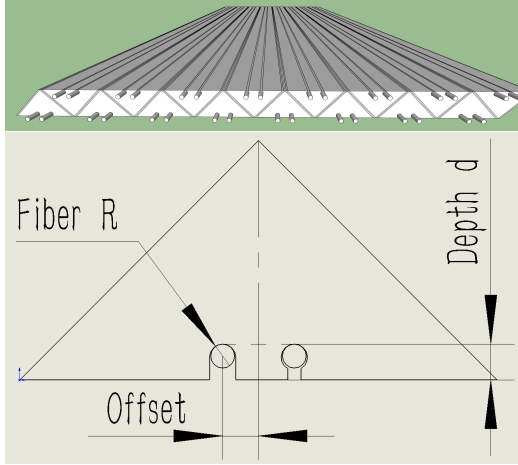


Figure 5: Scintillating detector structure. (Top) Arrangement of multiple scintillator bars. (Bottom) Parameters of the scintillator bar subject to optimization, including fiber radius ( $R$ ), groove depth ( $d$ ), and the offset of the fiber groove from the center. The two grooves depicted are a semi-circular groove (left) and an omega-shaped groove (right).

tial resolution. In our prior research, we developed and tested functional prototypes for different scintillator detector structures, each with an active area of  $15 \times 15 \text{ cm}^2$ [11]. Results show that the detector with triangular cross-section bars achieved a spatial resolution of 1.8 mm with a pitch of 1 cm, a significant improvement from the approximately 3 mm resolution of square cross-section bars.

A practical MST system requires large-area detectors exceeding  $50 \times 50 \text{ cm}^2$ . This necessity presents several engineering challenges: it demands longer scintillator bars, and subsequently compels us to address critical issues such as signal readout for large areas, modular design architecture, cost-effectiveness, and ease of installation. In contrast, the prototype detector's design does not satisfy these requirements. First, scintillator bars are read out by SiPMs at both ends, and an online coincidence logic between the two SiPMs is required. Consequently, signals from both SiPMs must be routed to the same readout module, forcing the long-distance transmission of unamplified analog signals. This not only complicates installation but also introduces significant noise, which in turn degrades the spatial resolution. Another critical flaw in the prototype detector is the lack of an encoded signal readout scheme. This leads to a high channel count, making the readout electronics a major cost driver.

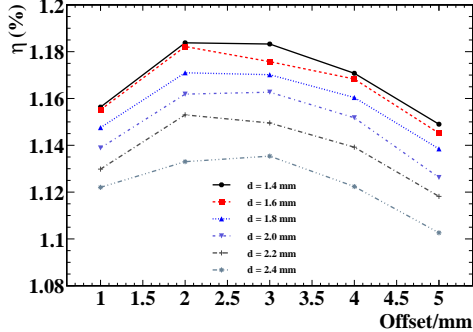
Accordingly, the detection plane structure depicted in the figure 5 was implemented in our design. Two optical fibers are embedded within a single scintillator bar. Each fiber is read out by a SiPM on only one end, with the opposite end mirrored to enhance total photon collection efficiency. All SiPMs are positioned on the same side of the scintillator array. This optimized structure simultaneously satisfies the requirement for coincidence measurements and resolves the design flaws present in the detector prototype.

The Geant4 simulation framework allows for a systematic study of how detector performance is influenced by key scintillator design parameters, ranging from the bar length and geometric features—such as fiber radius  $R$ , groove depth  $d$ , groove offset, and groove shape (semi-circular vs. omega)—to the physical coupling method at the scintillator-fiber interface (e.g., air coupling or optical grease coupling). Analysis of the simulation results focus on the photon collection efficiency  $\eta$ , defined as  $N_{\text{det}}/N_{\text{scint}}$ , where  $N_{\text{det}}$  is the photon count at the SiPM and  $N_{\text{scint}}$  is the total photon yield in the scintillator.

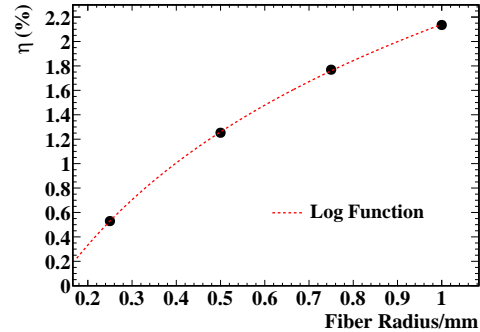
Figure 6 shows the variation of the photon collection efficiency  $\eta$  with key detector parameters, including the groove offset, depth, and fiber radius. In summary, Despite the relatively minor combined influence (within 10%) of parameters like offset, depth, coupling, and groove shape on  $\eta$ , the simulation results still allow for the determination of an optimal parameter set. A specific example is the groove offset, where  $\eta$  exhibits a non-monotonic relationship. This behavior led to the selection of 3 mm as the final parameter. Regarding the groove depth, the optimal strategy is to make it as shallow as possible while ensuring the fiber is properly embedded. We employed a semi-circular groove and air coupling, a choice that prioritizes maneuverability and straightforward installation.

However, the scintillator bar length and the fiber radius prove to be significantly more influential on the efficiency. The fiber radius governs the probability of photon capture and absorption by the WLS fiber, while the bar length dictates the degree of inherent attenuation during light transmission. The efficiency increases with the fiber radius and decreases with the scintillator bar length. Through a trade-off between cost and performance requirements, the final design parameters were chosen as a 60 cm scintillator bar length and a 0.75 mm fiber radius.

Finally, since a mirrored fiber end was adopted in our design to enhance photon collection efficiency, it is essential to evaluate its influence on the overall performance. We conducted an experiment using LED and wavelength-shifting (WLS) fiber, and compared the results with Geant4 simulations. Re-



(a) Results for depth  $d$  and groove offset.



(b) Results for fiber radius  $R$ .

Figure 6: Impact of selected parameters on the photon collection efficiency of the detector in Geant4 simulations.

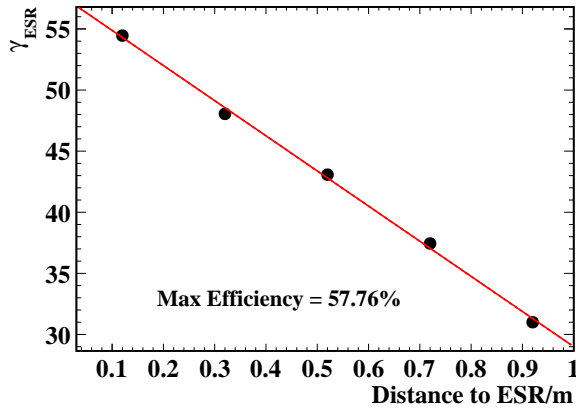


Figure 7: Test of the end reflection effect using an ESR film. The X axis is the distance between the LED and the ESR film, and the Y axis is the gain in photon count, obtained by comparing the signal amplitude with and without the ESR film attached to fiber end.

sults indicate that when a 1-meter fiber was irradiated by an LED at various positions, the relative gain in photon count provided by the end mirror (Enhanced Specular Reflector, ESR) progressively decreased from approximately 55% to 30% as the LED-to-mirror distance increased from 0 to 1 m. This result is consistent with the Geant4 simulation, confirming the effectiveness of the mirrored treatment applied to the fiber end.

The detector designed here incorporates wavelength-shifting fibers, which introduces a moderate increase in manufacturing cost. This is compensated for by the higher photon transmission efficiency of the fibers, which not only improves performance uniformity along the bar direction but also facilitates the extension of the detection area. Moreover, the use of fibers allows for the convenient and cost-effective splicing of multiple shorter scintillator bars to extend the active area, adding virtually no extra cost.

### 2.3.2. *Signal encoding*

The flux of cosmic ray particles is low, and a single incident particle, in most cases, will hit only two adjacent scintillator bars. This characteristic is exploited to implement an encoded signal readout scheme. Since each scintillator bar incorporates two optical fibers for light signal output, the signals from these two fibers can be routed to separate SiPMs, thereby enabling the encoding of the optical signal.

In our encoding scheme, 16 scintillator bars and their corresponding 32 optical fibers are grouped into a single module. The signals from every four fibers are input into one SiPM, thus requiring a total of eight SiPMs per encoding module. Compared to the previous prototype, this design achieves a compression ratio of 4:1. More specifically, the two fibers in each scintillator bar are designated as A (left) and B (right). Accordingly, the eight SiPMs are also divided into Group A and Group B, with each group exclusively receiving input from its corresponding set of fibers. A valid encoding scheme can be readily obtained by populating a  $4 \times 4$  table, defined by the four Group A and four Group B SiPMs, with the indices of the 16 scintillators. Table 1 provides an example mapping between SiPM numbers and scintillator numbers, for instance, the optical signals from the A and B fibers in Scintillator 0 are routed to SiPM A0 and B0, respectively. The global trigger signal for the encoding module is generated by the coincidence between the OR-ed outputs of Group A (A0-A3) and Group B (B0-B3).

Two critical rules must be observed when populating the encoding table with scintillator indices:

	B0	B1	B2	B3
A0	S0	S4	S8	S12
A1	S13	S1	S5	S9
A2	S10	S7	S2	S15
A3	S6	S14	S11	S3

Table 1: Encoding 16 scintillator strips to 8 SiPMs.

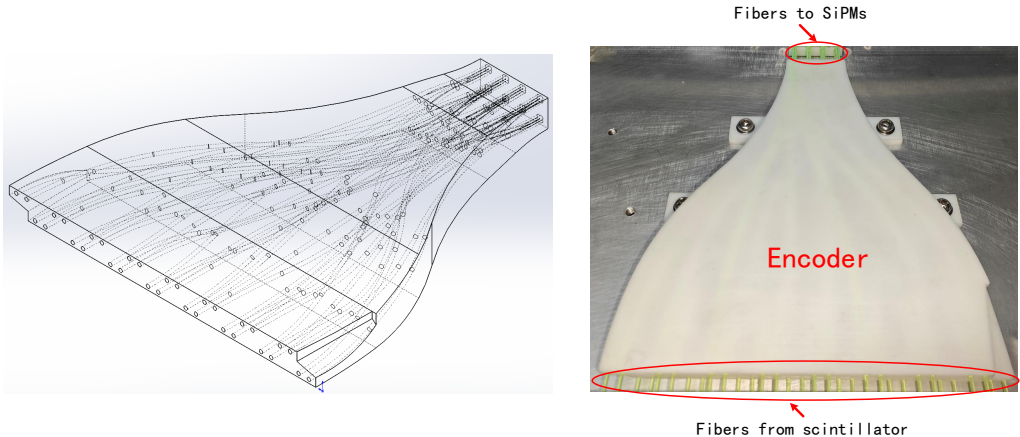


Figure 8: Encoder: internal structure and 3D-printed prototype.

1. Non-adjacency in rows/columns: adjacent scintillator indices must not be assigned to the same row or the same column. This constraint allows for the four fibers of two adjacent scintillators to be read by four different SiPMs, which avoids information loss in the encoding.
2. Rectangle corner constraint: no two pairs of adjacent indices may occupy all four corners of any rectangle within the table. This guarantees that whenever a coincidence signal from four SiPMs is present, the decoded result is unequivocal under such conditions.

In practical fiber encoding, the tangled fiber arrangement poses a significant challenge for detector assembly. Additionally, fibers exposed outside the assembly are highly vulnerable to breakage. To address these issues, an encoder is necessary to guide the fibers from the scintillators through precisely

designed internal passages, thereby organizing them into bundled clusters at the output for interfacing with the SiPM arrays. Accordingly, we designed and fabricated the encoder shown in Figure 8. The use of 3D design and printing overcame the limitations of traditional CNC machining by enabling the production of parts with intricate internal channels that would otherwise be impossible to manufacture.

An additional electronic-level encoding scheme was also proposed but ultimately abandoned[17]. This scheme aimed to digitize amplified signals from multiple SiPMs with a single ADC, but was rendered unnecessary by the substantial reduction in channel requirements achieved through fiber encoding.

The SiPMs feature a dark count rate on the order of 1 MHz. Furthermore, the use of triangular scintillator bars imposes a requirement to detect only about 10 photons for higher position resolution, which in turn necessitates a low signal threshold. Consequently, a coincidence measurement scheme using multiple SiPMs must be employed to suppress the false trigger rate effectively. This requirement is independent of the encoding scheme and is fundamental for reading out a bar with low photon yield. In fact, even a non-encoded design, such as our prototype detector, necessitates at least two SiPMs per bar. Therefore, the encoding scheme achieves a compression ratio of 1:4.

### 3. Construction and test for super layer

#### 3.1. Readout electronics

The performance of the readout electronics plays a key role in the detector and the overall MST system. The detector requires precise measurement of the photon count ratio between adjacent scintillator strips[12]. Furthermore, Geant4 simulations show that the photon count per individual SiPM ranges from 0 to 300. Therefore, the single-photon resolution within the 0-300 photon range is the primary performance for evaluating the readout electronics. Based on this requirement, we developed readout electronics[17], as shown in figure 9.

The front-end electronic board is built around the CITIROC 1A, which provides the front-end amplification for the SiPMs, and a Zynq-7000 SoC, which handles digital logic and serves as the data acquisition interface to the host PC. The electronic board is capable of providing temperature-compensated bias voltage to 32 SiPM channels, alongside performing signal amplification, shaping, as well as charge and time measurement for each

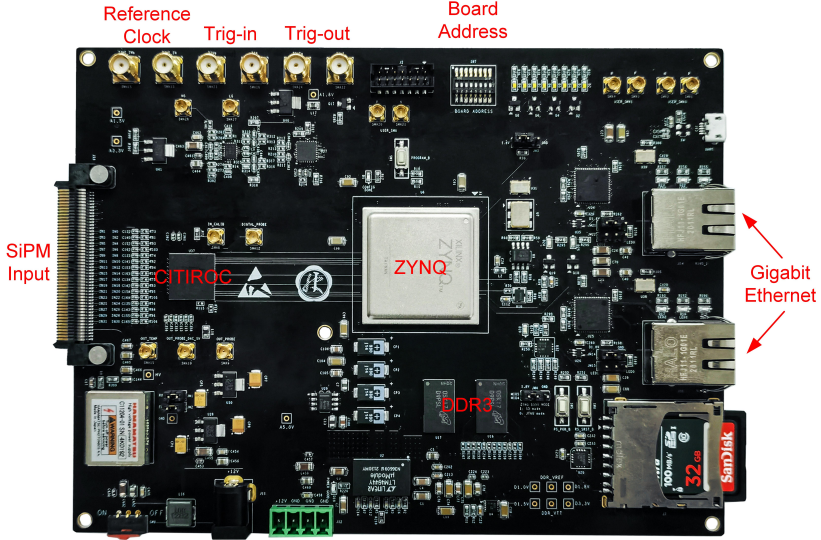


Figure 9: Electronic board designed for SiPM readout.

channel. Moreover, its charge measurement circuitry incorporates selectable high and low gains to adapt to varying dynamic ranges.

The readout electronics features a noise level as low as 0.45 fC, enabling excellent single-photon resolution. Figure 10 shows ADC spectrum of the Hamamatsu S13360-3075 SiPM under LED illumination, obtained with the readout electronics. A single-photon resolution of  $17\sigma$  is achieved, as shown in the figure.

The electronic boards are designed not only to meet the photon detection requirements of individual detection planes but also to support system-level functions for the multi-board MST setup, including trigger logic, inter-board communication, and time synchronization. As shown in Figure 11, all electronic boards are connected in a daisy-chain topology. Data packets are transferred sequentially between boards through Ethernet cables, while inter-board event handshaking is implemented via the TIN and TOUT signal lines. When a board is triggered internally by a cosmic ray event, it sets its TOUT output to a high level. An event is considered confirmed and is recorded by a board only if its TIN input receives a high-level signal within 150 ns after its own internal trigger. Different test functions can be realized by configuring the logic relationship between TIN and TOUT, which will be described in section 3.4.

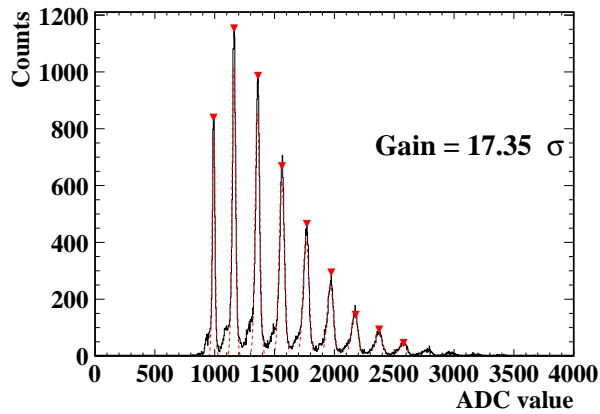


Figure 10: Single-photon resolution test of the readout board: response of a Hamamatsu S13360-3075 SiPM to LED light.

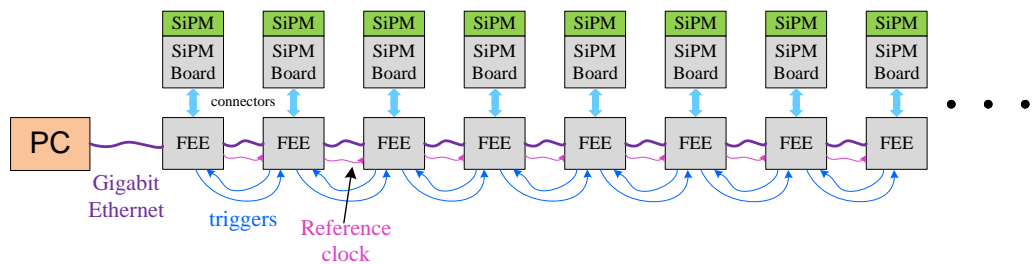


Figure 11: Daisy chain topology across multiple electronic boards.

The distributed nature of the electronics system necessitates precise timing coordination to ensure data consistency. To compensate for clock drift between individual boards, a common 1 Hz reference signal is distributed throughout the system. Each board records the arrival time of this synchronized pulse, enabling offline calibration and alignment of measurement timestamps across all units. This synchronization is critical for accurately reconstructing cosmic ray trajectories that involve triggers from multiple detection planes.

In addition to the SiPM FEE board, we developed a mounting board that can accommodate up to 32 SiPMs, corresponding to four encoding modules. These are paired with custom 3D-printed couplers to ensure precise alignment between the wavelength-shifting fibers and the SiPMs. Each encoding module incorporates a centrally located temperature sensor for real-time monitoring and compensation of its eight SiPMs. In practice, only three of the four modules are utilized in the current setup.

### *3.2. Detector fabrication*

We selected the EJ-200 scintillator, Kuraray Y11 wavelength shift fibers, and Hamamatsu S13360-3075 SiPMs to construct the muon detector. After cutting the scintillator slab into isosceles triangular strips with a base of 20 mm and a height of 10 mm, the strips were grooved, polished, and wrapped with Tyvek paper to reflect the fluorescent photons. We assembled the module by aligning the scintillator strips with a center-to-center pitch of 11 mm, clamping them with a fixture, and maintaining a 1 mm inter-strip gap for the Tyvek wrapper. The WLS fibers were inserted, with one end anchored to an ESR reflector and the other end passed through the encoder for optical coupling to the SiPMs.

Figure 12 presents the layout and a photograph of a super layer within the dark box. Each dark box contains a super layer, formed by two orthogonal X and Y detection planes. Each plane contains 48 scintillator strips (60 cm long), giving it an effective area of 53 cm  $\times$  60 cm, with the super layer's active area being the 53 cm  $\times$  53 cm overlap. The 48 strips are grouped into three encoding modules, read out by 24 SiPMs and electronic channels. Each plane interfaces with one electronic board, which uses 24 of its 32 channels.

### *3.3. Raw data processing*

With the assembly of multiple detectors completed, we performed a series of processing steps on the raw readout signals, namely time calibration, event

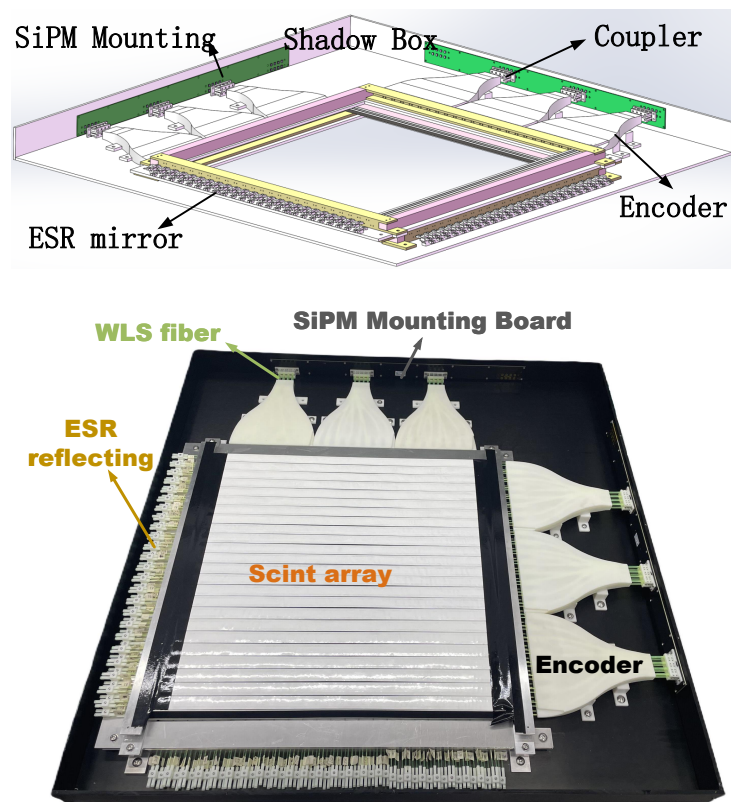


Figure 12: A super layer within a dark box: comprising two detection planes, each constructed from three encoding modules.

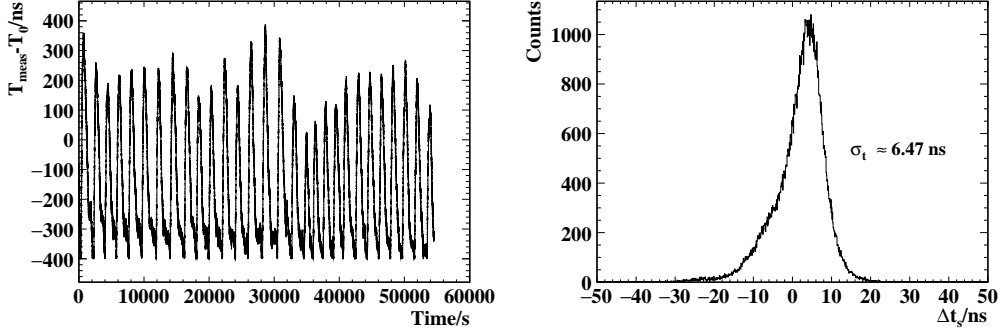


Figure 13: Timing synchronization of the readout electronic boards. (Left) Measured period of the common 1 Hz pulse over time. (Right) Corrected time difference for a single cosmic event measured by two boards.

matching, channel calibration, signal decoding, and position reconstruction.

*Time calibration.* As described in the previous section, system-wide synchronization is achieved by distributing a common 1 Hz reference pulse and comparing its recorded arrival times across all electronic boards. This procedure compensates for clock frequency variations among individual units. The left panel of figure 13 shows the time interval between two consecutive pulses recorded by a representative board as a function of measurement time. After time calibration, the timestamp difference between any two boards for the same physical event is within 100 ns, as demonstrated in the right panel of the figure.

*Event matching.* The event reconstruction process is performed in two sequential stages: intra-board and inter-board matching. In the intra-board stage, the three raw data streams produced by each electronic board—high-gain charge, low-gain charge, and timing information—are merged into a single coherent data stream. This is accomplished by assigning a common trigger identifier that is shared internally across all three measurement channels within the board. The inter-board stage identifies events from different readout boards that were produced by the same cosmic ray. Events are considered coincident if their calibrated timestamps differ by less than 100 ns ( $\Delta t < 100 \text{ ns}$ ).

*Channel calibration.* The channel calibration was conducted in two main steps, as shown in figure 14. First, establish the relationship between the

High-Gain (HG) and Low-Gain (LG) ADC values and the SiPM photon counts. This correspondence enables the definition of channel-by-channel thresholds and triggers an automatic switch to the LG readout upon saturation of the HG channel during data analysis. To achieve this, the distribution of HG ADC values at low photon levels was initially plotted and correlated with SiPM photon counts. Subsequently, the relationship between LG ADC values and the photon counts derived from HG was plotted using high-intensity data, thereby establishing a complete HG–LG–photon count correspondence.

Second, calibrate the response non-uniformity across different scintillator units. The non-uniformity arise from two primary sources: differences in the electronics (such as amplifiers and ADCs) and variations in scintillation units (e.g., light yield of scintillators and optical coupling between the fibers, scintillators, and SiPMs). We fitted the ADC spectrum from cosmic ray tests with the spectrum from Geant4 simulations, using the scale factor  $k_{\text{fit}}$  to quantify the non-uniformity across different scintillators and readout channels.  $k_{\text{fit}}$  is applied to calibrate and normalize the variations across different scintillators and corresponding readout channels.

*Decoding.* The most straightforward decoding approach identifies the four SiPMs with the highest calibrated signal amplitudes and determines the hit position using a pre-defined lookup table presented in table 1. However, this direct decoding scheme is highly susceptible to interference from optical crosstalk between adjacent scintillator strips. This vulnerability arises because low photon counts in a SiPM can have two distinct origins: genuine but weak energy deposition from a muon, or spurious signals from crosstalk. The algorithm’s inability to reliably distinguish between these two cases is the fundamental reason for decoding errors. While signals from true weak depositions are valuable for position reconstruction, mistakenly incorporating crosstalk signals can lead to significant errors in the final position determination.

To address this issue, a more robust decoding scheme has been implemented. The new scheme employs a higher threshold (typically around 70 p.e.), where any channel exceeding this threshold is considered to register a true signal rather than crosstalk. When exactly four channels are activated, the corresponding scintillator strips are directly identified using the lookup table, and the position is calculated using the charge centroid method. If fewer than four channels are triggered, the scheme first identifies the strip

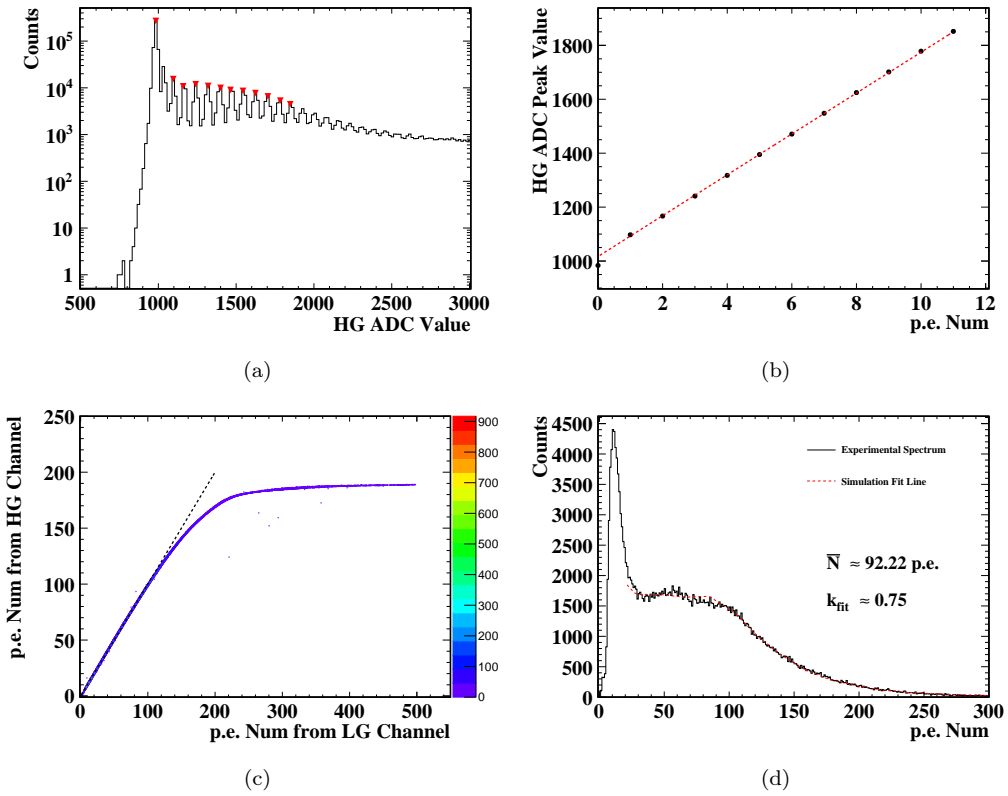


Figure 14: Channel Calibration. (a): HG channel spectrum under low intensity. (b): Linear fit to the correlation between HG ADC Values and SiPM photon-electron counts. (c): LG-HG detected p.e. counts correlation, nonlinearity shown in HG at p.e. counts  $> 100$ . (d): Measured cosmic ray photon spectrum fitted by Geant4 simulation spectrum (red dashed line), with the scale factor  $k_{\text{fit}}$  applied for normalization.

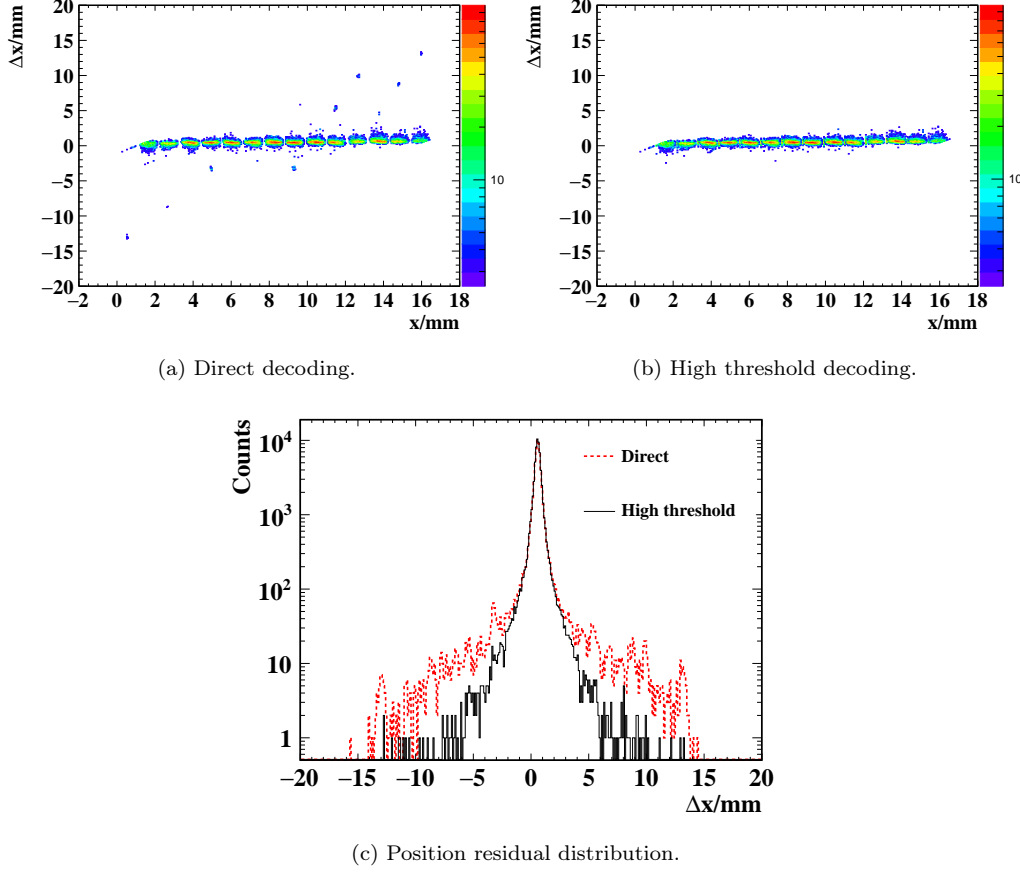


Figure 15: Comparison for different decoding schemes.

corresponding to the two strongest signals, then compares the signals from the two adjacent strips and selects the one with the higher signal for centroid-based positioning. This approach ensures both positioning accuracy and decoding reliability.

We evaluated the performance of two encoding schemes by integrating the encoding module into a cosmic ray test system. Two prototype detectors, which operated without signal encoding, provided reference cosmic ray triggers and precise incident position information to the module under test. As shown in Figure 15, the resulting position residual distributions demonstrate that the new high-threshold approach significantly reduces misidentification probability compared to direct decoding.

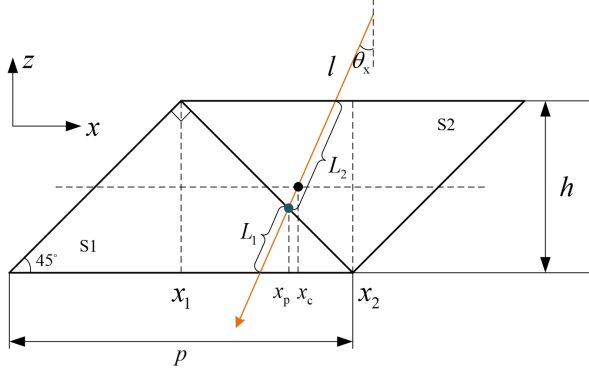


Figure 16: Positioning and correction via the centroid method.

*Position reconstruction.* The charge centroid method reconstructs the intersection point  $x_p$  where the muon track crosses the boundary of the scintillator strip, neglecting the finite gaps between adjacent strips. Given the incident angle, this can be transformed into the intercept coordinate at the center of the detection plane  $x_c$ , which is described by the following equation:

$$\begin{aligned} x_p &= \frac{x_1 \cdot L_1 + x_2 \cdot L_2}{L_1 + L_2} = x_1 + \eta \cdot p \\ x_c &= x_p + (\eta - 0.5) \cdot h \cdot \tan \theta_x \end{aligned} \quad (2)$$

, where  $x_1$  is the reference strip position,  $p = x_2 - x_1$  the strip pitch,  $\eta = L_2/(L_1 + L_2)$  the charge-sharing fraction,  $h$  the height of scintillator bar, and  $\theta_x$  the muon zenith angle.

The photoelectron count  $N$  registered by a SiPM is proportional to the energy deposition  $E$  of the traversing muon. For minimum-ionizing particles (MIPs),  $E$  is approximately proportional to the path length  $L$  within the scintillator bar. Consequently, the ratio of path lengths  $L_1/L_2$  can be estimated from the measured signal ratio  $N_1/N_2$  of two adjacent strips.

Each detection plane independently provides a preliminary hit position  $x_p$  based solely on the charge-sharing fraction  $\eta$  between neighboring strips. Using the coarse positions  $x_p$  from multiple planes, the muon's incident angle  $\theta_x$  is reconstructed. This angle is then applied as a geometric correction, yielding the refined hit coordinate  $x_c$ .

However, the coordinate  $x_c$  obtained above does not account for the finite gap between adjacent scintillator bars. Geant4 simulations reveal a

correlation between the residual offset  $\Delta x$  and the charge-sharing fraction  $\eta$ , which can be corrected using a linear function [12]. The three-step procedure—centroid positioning, angle correction, gap correction—yields the final accurate position.

### 3.4. Detector performance

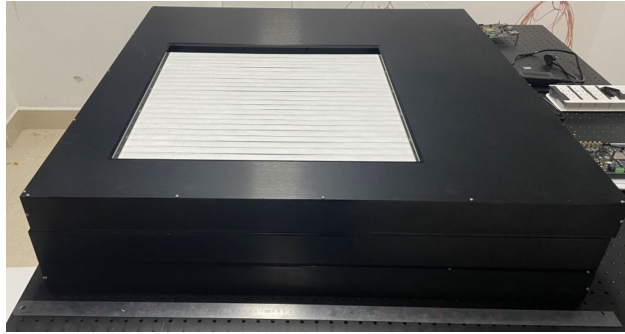
With the initial processing of the raw signals completed, we can now proceed to assess the performance of the multi-layer detection system. Its key parameters, including detection efficiency, position, and spatial resolution, was characterized using a three-super-layer configuration under different coincidence logic.

*Detection efficiency.* For the measurement of detection efficiency, the coincidence signal from the top and bottom layers was used as the trigger input for the middle layer, as shown in figure 17b. Thus, the signals recorded in the middle layer represented a three-fold coincidence among all three super-layers, while the top and bottom layers each registered a two-fold coincidence signal.

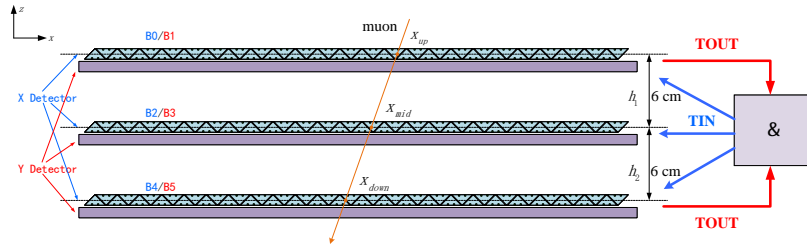
Let  $N_A$  be the count of coincidence events between the top and bottom layers, and  $N_B$  the total count of three-fold coincidences (top, middle, bottom). The detection efficiency of the middle layer is then  $\epsilon_{\text{mid}} = N_B/N_A$ . During a 24-hour measurement period, the recorded counts were  $N_A = 239,963$  and  $N_B = 233,882$ . The resulting detection efficiency for the middle layer  $\epsilon_{\text{mid}}$  was determined to be 97.47%. The detection efficiency reported here is a comprehensive value that incorporates the intrinsic detection efficiency of the detectors, the data transmission efficiency of the readout electronics, and the efficiency of the multi-layer event matching process.

*Temporal resolution.* The measurement of both temporal and spatial resolution requires events from a three-fold coincidence across the detector layers. To achieve this, the logic connections between the electronic boards are implemented as illustrated in figure 17c. The TOUT signals from the three layers are combined in coincidence to generate a global validation signal for the entire stack.

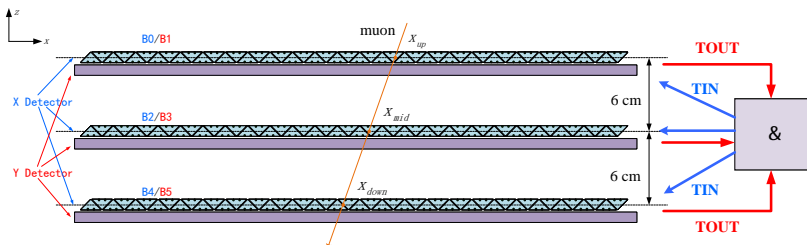
In order to get precise timing, a final calibration step is necessary after the initial time correction and event matching. This step incorporates corrections for three key factors: inter-channel timing variations within the front-end electronics, the propagation delay of photons along the wavelength shift fibers



(a) Experimental setup: a three-super-layer stack.



(b) Logic of the efficiency test across layers.



(c) Logic of the spatial/temporal resolution test across layers.

Figure 17: Test system composed of three super layers.

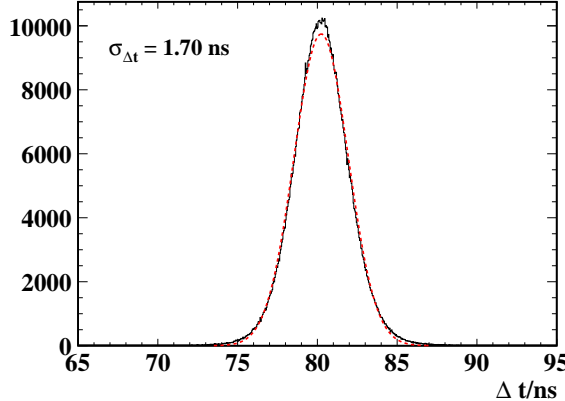


Figure 18: Distribution of the calibrated time difference between the top and bottom detection planes.

(which depends on the hit position), and the time of flight of the muon through the entire detector system. As shown in the figure 18, the final time resolution, characterized by the distribution of time differences between the top and bottom detection layers for identical events,  $\Delta t = t_{\text{top}} - t_{\text{bottom}}$ , achieves a  $\sigma_{\Delta t}$  of 1.7 ns. The single detection plane timing resolution is therefore inferred to be  $\sigma_t = 1.2$  ns.

*Spatial resolution.* The same logic configuration from the temporal resolution test was used to measure the detector’s spatial resolution. The test system determines the trajectory and incident angle  $\theta$  of muons. Therefore, equation 2 provides the corrected impact position  $x_c$  at the center of the detection plane. In addition, the hit position resolution is further corrected for the inter-strip gaps, as determined from Geant4 simulations[12].

The final residual distribution for the middle-layer position measurement, after incorporating all the aforementioned corrections, is shown in figure 19. The standard deviation of the Gaussian peak in the figure is 1.24 mm. Assuming that each detector layer has an identical spatial resolution of  $\sigma_x$ , and applying the error propagation formula, the resulting residual  $\sigma_{\Delta x}$  for the

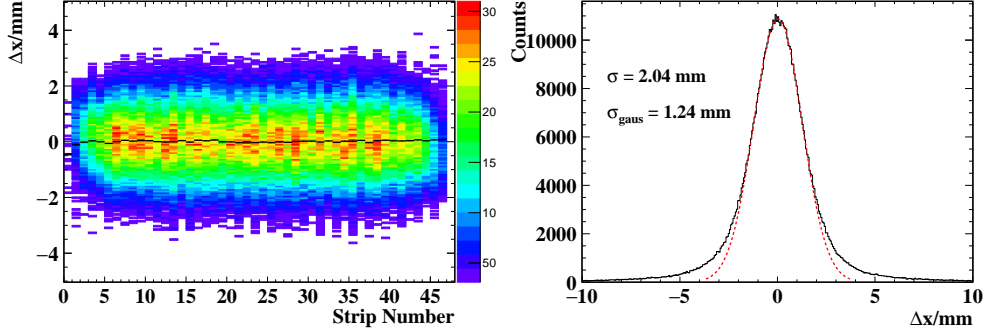


Figure 19: Position residual distribution of the middle layer detector. (Left): Residual distribution as a function of the scintillator strip index. (Right): Residual distribution of all strips.

middle layer is given by:

$$\begin{aligned}
 x_{\text{mid, fit}} &= \frac{h_2 \cdot x_{\text{u}} + h_1 \cdot x_{\text{d}}}{h_1 + h_2}, \quad \Delta x = x_{\text{mid, meas}} - x_{\text{mid, fit}} \\
 \sigma_{\Delta x} &= \sqrt{\sigma_x^2 \left( \frac{h_1}{h_1 + h_2} \right)^2 + \sigma_x^2 \left( \frac{h_2}{h_1 + h_2} \right)^2 + \sigma_x^2} \\
 &= \frac{\sqrt{2h_1^2 + 2h_1h_2 + 2h_2^2}}{h_1 + h_2} \sigma_x = 1.22 \sigma_x
 \end{aligned} \tag{3}$$

, where  $h_1$  and  $h_2$  are the distances between the two detector layers, as labeled in figure 17c,  $x_{\text{u}}$  and  $x_{\text{d}}$  denote the position measurements from the upper and lower detector layers, respectively. Therefore, the measured spatial resolution of the detector is 1.0 mm. Given that the pitch (center-to-center distance between scintillator bars) is 11 mm, the normalized resolution  $\sigma_x/p$  is calculated to be 0.09.

For scintillator detectors with a triangular cross-section, the normalized spatial resolution  $\sigma_x/p$  is typically around 0.2, as demonstrated in systems such as MU-RAY[18], CRIPT[19], and LUMIS[20]. While improved designs have further reduced this value to approximately 0.13 in some advanced detectors[21], our detector achieves a significantly lower  $\sigma_x/p$  of 0.09. This result highlights a clear performance advantage over conventional designs. The enhancement is attributed to concurrent improvements in photon collection efficiency, position reconstruction algorithms, and electronic noise suppression.

## 4. MST system

### 4.1. System construction

The Muon Scattering Tomography (MST) system consists of an upper tracker and a lower tracker, comprising four super layers in total. These super layers collectively contain 8 detection planes, 24 encoding modules, 384 scintillator strips, 768 optical fibers, 192 SiPMs, and 8 readout electronic boards.

During assembly, we established a quality control system to monitor key parameters such as scintillator light yield and fiber transmission efficiency, and performed calibration of the SiPM temperature compensation and the gain of each electronic channel. These fundamental efforts ensure the reliable performance of the imaging system.

After assembling the four detectors, we arranged them at different heights, thus finalizing the construction of the MST system, as shown in figure 20. The four detector layers are arranged with a pairwise separation of around 90 cm. The spacing between the two central layers is sufficient to accommodate other detectors under test (DUT). This configuration allows the system to perform scattering tomography intrinsically, while also enabling it to function as a cosmic ray telescope that provides muon triggers and track information for the DUTs.

### 4.2. Imaging results

The fully assembled MST system was employed for imaging tests. Within the imaging volume, we placed 2 cm cubic blocks of tungsten, lead, and aluminum, arranged in distinct patterns as shown in Figure 21. Data acquisition spanned approximately 10 days, accumulating about  $2.5 \times 10^5$  events for subsequent analysis.

The Point of Closest Approach (PoCA) algorithm was used to reconstruct the objects within the imaging volume. As shown in figure 22, even the smallest aluminum block (a low-Z material) measuring  $2 \times 2 \times 2$  cm<sup>3</sup> is clearly reconstructed. The imaging analysis for the tungsten blocks is shown in figure 22b, achieving a signal-to-background ratio (S/B) of 8.4 and an  $\varepsilon_{\text{PSF}}$  of about 0.35 cm. This result demonstrates the promising imaging capabilities of the developed MST system.

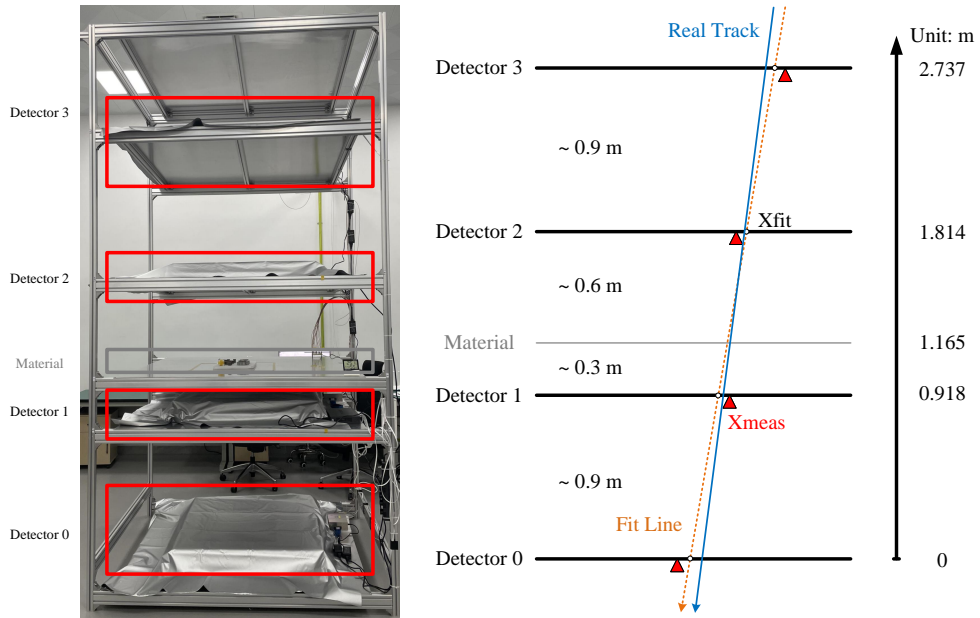


Figure 20: Muon scattering tomography system. Additionally serves as a cosmic ray telescope, providing cosmic ray trigger and track information.

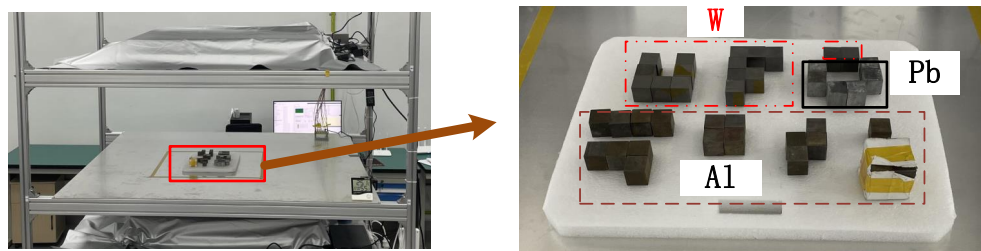
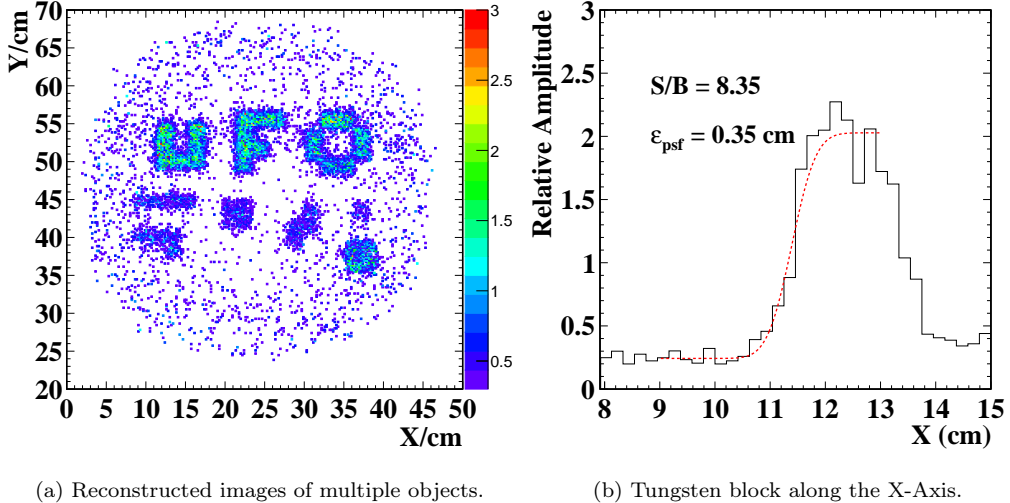


Figure 21: Objects placed in the imaging volume. The letters "UFO" are composed of tungsten and lead blocks, while the Tetris-shaped pattern below is made of aluminum. Each individual block measures  $2 \times 2 \times 2 \text{ cm}^3$ .



(a) Reconstructed images of multiple objects. (b) Tungsten block along the X-Axis.

Figure 22: Material distribution reconstructed by the MST system using the PoCA algorithm

## 5. Conclusion and outlook

We present the full development of a cosmic ray muon scattering tomography setup, covering its design, simulation, construction, performance characterization, and imaging validation. The core of this setup is a large-area, high-spatial-resolution scintillating detector, which was systematically optimized through Geant4 simulations. Key design parameters including a triangular bar geometry with an 11 mm pitch, a fiber encoding scheme, and the low-noise readout electronics, were meticulously engineered to achieve a spatial resolution of 1.0 mm and a detection efficiency of 97.47% per detection plane. This results in a large effective detection area of  $53 \text{ cm} \times 53 \text{ cm}$  for each super layer. Notably, the system achieves a normalized spatial resolution  $\sigma_x/p$  of 0.09, representing a clear improvement over conventional scintillator-based MST systems, which typically reach around 0.2.

The fully assembled system's imaging capability was successfully demonstrated by clearly reconstructing small test objects ( $2 \times 2 \times 2 \text{ cm}^3$  cubes) made of various materials, including low-Z aluminum. The results confirm that the enhanced spatial resolution directly translates to superior image quality, characterized by a high signal-to-noise ratio and sharp boundaries, as predicted by our initial simulations.

The successful construction and validation of this MST setup open several promising future directions. While the PoCA algorithm has proven effective for initial imaging, the high-quality track data from our system is well-suited for more advanced reconstruction algorithms, such as Maximum Likelihood/Expectation Maximization (ML/EM) or machine learning-based methods. These algorithms have the potential to further enhance image fidelity and material discrimination capabilities. Due to the unique geometric configuration of plastic scintillators requires specialized processing techniques. To address this challenge, we are investigating alternative approaches using liquid scintillators, which exhibit luminescent properties similar to plastics, offer easier shaping and processing, and show promise for enhancing scalability and reducing costs in the large-area MST arrays.

### Acknowledgments

This research work is supported by the National Key R&D Program of China, No. 2023YFA1606903, and National Natural Science Foundation of China, No. 12375185, and Anhui Provincial Natural Science Foundation under Grant No. 2208085MA12.

We gratefully acknowledge the financial support and the provision of experimental facilities by the Institute of Modern Physics, Chinese Academy of Sciences. The scintillators were processed and assembled into detectors at the University of Science and Technology of China (USTC), and the complete MST system was subsequently installed and tested at the Huizhou Campus of the Institute of Modern Physics.

### References

- [1] G. Ambrosi, F. Ambrosino, R. Battiston, A. Bross, S. Callier, F. Cassese, G. Castellini, R. Ciaranfi, F. Cozzolino, R. D'Alessandro, C. de La Taille, G. Iacobucci, A. Marotta, V. Masone, M. Martini, R. Nishiyama, P. Noli, M. Orazi, L. Parascandolo, P. Parascandolo, G. Passeggio, R. Peluso, A. Pla-Dalmau, L. Raux, R. Rocco, P. Rubinov, G. Saracino, G. Scarpati, G. Sekhniaidze, P. Strolin, H. Tanaka, M. Tanaka, P. Trattino, T. Uchida, I. Yokoyama, The mu-ray project: Volcano radiography with cosmic-ray muons, Nuclear Instruments and Methods in Physics Research Section A: Accelerators, Spectrometers, Detectors and Associated Equipment 628 (1) (2011) 120–123, vCI 2010. doi:<https://doi.org/10.1016/j.nima.2010.06.299>.

- [2] D. Varga, G. Nyitrai, G. Hamar, G. Galgócz, L. Oláh, H. Tanaka, T. Ohminato, Detector developments for high performance muography applications, Nuclear Instruments and Methods in Physics Research Section A: Accelerators, Spectrometers, Detectors and Associated Equipment 958 (2020) 162236, proceedings of the Vienna Conference on Instrumentation 2019. doi:<https://doi.org/10.1016/j.nima.2019.05.077>.
- [3] K. Morishima, M. Kuno, A. Nishio, N. Kitagawa, Y. Manabe, M. Moto, F. Takasaki, H. Fujii, K. Satoh, H. Kodama, K. Hayashi, S. Odaka, S. Procureur, D. Attié, S. Bouteille, D. Calvet, C. Filosa, P. Magnier, I. Mandjavidze, M. Riallot, B. Marini, P. Gable, Y. Date, M. Sugiura, Y. Elshayeb, T. Elnady, M. Ezzy, E. Guerriero, V. Steiger, N. Serikoff, J.-B. Mouret, B. Charlès, H. Helal, M. Tayoubi, Discovery of a big void in Khufu's Pyramid by observation of cosmic-ray muons, *Nature* 552 (7685) (2017) 386–390. doi:10.1038/nature24647.
- [4] W. Priedhorsky, K. Borozdin, G. Hogan, C. Morris, A. Saunders, L. Schultz, M. Teasdale, Detection of high-z objects using multiple scattering of cosmic ray muons, *Review of Scientific Instruments* 74 (10 2003). doi:10.1063/1.1664345.
- [5] K. N. Borozdin, G. E. Hogan, C. Morris, W. C. Priedhorsky, A. Saunders, L. J. Schultz, M. E. Teasdale, Radiographic imaging with cosmic-ray muons, *Nature* 422 (6929) (2003) 277–277. doi:10.1038/422277a.
- [6] L. J. Schultz, G. S. Blanpied, K. N. Borozdin, A. M. Fraser, N. W. Hengartner, A. V. Klimenko, C. L. Morris, C. Orum, M. J. Sosong, Statistical reconstruction for cosmic ray muon tomography, *IEEE Transactions on Image Processing* 16 (8) (2007) 1985–1993. doi:10.1109/TIP.2007.901239.
- [7] L. Schultz, K. Borozdin, J. Gomez, G. Hogan, J. McGill, C. Morris, W. Priedhorsky, A. Saunders, M. Teasdale, Image reconstruction and material z discrimination via cosmic ray muon radiography, *Nuclear Instruments and Methods in Physics Research Section A: Accelerators, Spectrometers, Detectors and Associated Equipment* 519 (3) (2004) 687–694. doi:<https://doi.org/10.1016/j.nima.2003.11.035>.
- [8] C. L. Morris, K. Borozdin, J. Bacon, E. Chen, Z. Lukić, E. Milner, H. Miyadera, J. Perry, D. Schwellenbach, D. Aberle, W. Dreesen, J. A.

Green, G. G. McDuff, K. Nagamine, M. Sossong, C. Spore, N. Toleman, Obtaining material identification with cosmic ray radiography, *AIP Advances* 2 (4) (2012) 042128. doi:10.1063/1.4766179.

[9] Y. Wang, Z. Zhang, S. Liu, Z. Shen, C. Feng, J. Liu, Y. Liu, A High Spatial Resolution Muon Tomography Prototype System Based on Micromegas Detector, *IEEE Transactions on Nuclear Science* 69 (1) (2022) 78–85. doi:10.1109/TNS.2021.3137415.

[10] L. Cox, P. Adsley, J. O’Malley, S. Quillin, C. Steer, C. Clemett, Detector requirements for a cosmic ray muon scattering tomography system, in: 2008 IEEE Nuclear Science Symposium Conference Record, 2008, pp. 706–710. doi:10.1109/NSSMIC.2008.4775227.

[11] Z. Liang, T. Hu, X. Li, Y. Wu, C. Li, Z. Tang, A cosmic ray imaging system based on plastic scintillator detector with sipm readout, *Journal of Instrumentation* 15 (07) (2020) C07033. doi:10.1088/1748-0221/15/07/C07033.

[12] T. Hu, Z. Liang, X. Li, C. Li, Z. Tang, Y. Wu, Development of a plastic scintillation detector for muon scattering imaging, *Journal of Instrumentation* 15 (11) (2020) P11017. doi:10.1088/1748-0221/15/11/P11017.

[13] S. Chatzidakis, S. Chrysikopoulou, L. Tsoukalas, Developing a cosmic ray muon sampling capability for muon tomography and monitoring applications, *Nuclear Instruments and Methods in Physics Research Section A: Accelerators, Spectrometers, Detectors and Associated Equipment* 804 (2015) 33–42. doi:https://doi.org/10.1016/j.nima.2015.09.033.

[14] T. R. Corle, G. S. Kino, Chapter 1 - introduction, in: T. R. Corle, G. S. Kino (Eds.), *Confocal Scanning Optical Microscopy and Related Imaging Systems*, Academic Press, Burlington, 1996, pp. 1–66. doi:https://doi.org/10.1016/B978-012408750-7/50009-4.

[15] J. E. Barnes, Characteristics and control of contrast in ct., *RadioGraphics* 12 (4) (1992) 825–837, pMID: 1636042. arXiv:https://doi.org/10.1148/radiographics.12.4.1636042, doi:10.1148/radiographics.12.4.1636042.

[16] V. Antonuccio, M. Bandieramonte, U. Becciani, D. Bonanno, G. Bonanno, D. Bongiovanni, P. Fallica, S. Garozzo, A. Grillo, P. La Rocca,

E. Leonora, F. Longhitano, D. Lo Presti, D. Marano, O. Parasole, C. Pugliatti, N. Randazzo, F. Riggi, S. Riggi, G. Romeo, M. Romeo, G. Russo, G. Santagati, M. Timpanaro, G. Valvo, The muon portal project: Design and construction of a scanning portal based on muon tomography, *Nuclear Instruments and Methods in Physics Research Section A: Accelerators, Spectrometers, Detectors and Associated Equipment* 845 (2017) 322–325, proceedings of the Vienna Conference on Instrumentation 2016. doi:<https://doi.org/10.1016/j.nima.2016.05.006>.

[17] Z. Wang, Y. Wang, X. Li, Y. Zhao, Y. Liang, Z. Liang, Y. Zhang, Z. Tang, C. Li, Electronics design for a muon imaging system using triangular plastic scintillators with wls fiber readouts, *Journal of Instrumentation* 19 (02) (2024) P02033. doi:[10.1088/1748-0221/19/02/P02033](https://doi.org/10.1088/1748-0221/19/02/P02033).

[18] F. Ambrosino, A. Anastasio, D. Basta, L. Bonechi, M. Brianzi, A. Bross, S. Callier, A. Caputo, R. Ciaranfi, L. Cimmino, R. D'Alessandro, L. D'Auria, C. D. L. Taille, S. Energico, F. Garufi, F. Giudicepietro, A. Lauria, G. Macedonio, M. Martini, V. Masone, C. Mattone, M. C. Montesi, P. Noli, M. Orazi, G. Passeggi, R. Peluso, A. Pla-Dalmau, L. Raux, P. Rubinov, G. Saracino, E. Scarlini, G. Scarpato, G. Sekhniadze, O. Starodubtsev, P. Strolin, A. Taketa, H. K. M. Tanaka, A. Vanzanella, L. Viliani, The MU-RAY project: Detector technology and first data from Mt. Vesuvius, *Journal of Instrumentation* 9 (02) (2014) C02029–C02029. doi:[10.1088/1748-0221/9/02/C02029](https://doi.org/10.1088/1748-0221/9/02/C02029).

[19] V. Anghel, J. Armitage, F. Baig, K. Boniface, K. Boudjemline, J. Bueno, E. Charles, P.-L. Drouin, A. Erlandson, G. Gallant, R. Gazit, D. Godin, V. Golovko, C. Howard, R. Hydomako, C. Jewett, G. Jonkmans, Z. Liu, A. Robichaud, T. Stocki, M. Thompson, D. Waller, A plastic scintillator-based muon tomography system with an integrated muon spectrometer, *Nuclear Instruments and Methods in Physics Research Section A: Accelerators, Spectrometers, Detectors and Associated Equipment* 798 (2015) 12–23. doi:[10.1016/j.nima.2015.06.054](https://doi.org/10.1016/j.nima.2015.06.054).

[20] X. Luo, Q. Wang, K. Qin, H. Tian, Z. Fu, Y. Zhao, Z. Shen, H. Liu, Y. Fu, G. Liu, K. Yao, X. Qian, J. Rong, W. Zhang, X. Luo, C. Liu, X. Tian, M. Yu, F. Wu, J. Chen, J. Liu, Z. Liu, Development and commissioning of a compact Cosmic Ray Muon imaging prototype, *Nuclear Instruments and Methods in Physics Research Section A: Accelerators, Spectrometers, Detectors and Associated Equipment* 845 (2017) 322–325, proceedings of the Vienna Conference on Instrumentation 2016. doi:<https://doi.org/10.1016/j.nima.2016.05.006>.

ators, Spectrometers, Detectors and Associated Equipment 1033 (2022) 166720. doi:10.1016/j.nima.2022.166720.

[21] G. Saracino, L. Amato, F. Ambrosino, G. Antonucci, L. Bonechi, L. Cimmino, L. Consiglio, R. D. . Alessandro, E. D. Luzio, G. Minin, P. Noli, L. Scognamiglio, P. Strolin, A. Varriale, Imaging of underground cavities with cosmic-ray muons from observations at Mt. Echia (Naples), *Scientific Reports* 7 (1) (2017) 1181. doi:10.1038/s41598-017-01277-3.